Non-destructive Testing of Composite Fibre Materials with Hyperspectral Imaging - Evaluative Studies in the EU H2020 FibreEUse Project

Yijun Yan, *Member, IEEE,* Jinchang Ren, *Senior Member, IEEE,* Huan Zhao, James F.C. Windmill, *Senior Member, IEEE,* Winifred Ijomah, Jesper de Wit, and Justus von Freeden

Abstract: **Through capturing spectral data from a wide frequency range along with the spatial information, hyperspectral imaging (HSI) can detect minor differences in terms of temperature, moisture and chemical composition. Therefore, HSI has been successfully applied in various applications, including remote sensing for security and defense, precision agriculture for vegetation and crop monitoring, food/drink, and pharmaceuticals quality control. However, for condition monitoring and damage detection in carbon fibre reinforced polymer (CFRP), the use of HSI is a relatively untouched area, as existing non-destructive testing (NDT) techniques focus mainly on delivering information about physical integrity of structures but not on material composition. To this end, HSI can provide a unique way to tackle this challenge. In this paper, with the use of a near-infrared HSI camera, applications of HSI for the non-destructive inspection of CFRP products are introduced, taking the EU H2020 FibreEUse project as the background. Technical challenges and solutions on three case studies are presented in detail, including adhesive residues detection, surface damage detection and Cobot based automated inspection. Experimental results have fully demonstrated the great potential of HSI and related vision techniques for NDT of CFRP, especially the potential to satisfy the industrial manufacturing environment.**

***Index Terms*—Hyperspectral imaging (HSI); non-destructive inspection; carbon fibre reinforced polymer (CFRP); H2020.**

I. Introduction

Many sectors, including aerospace, maritime transportation, sports, and civil engineering, use carbon fiber-reinforced polymer composites (CFRP) as structural materials because of its unique properties of lightweight, high stiffness/strength and damping resistance [1, 2], as illustrated in Fig. 1(a). Components and products based on composites often have a lifespan of fewer than 20 to 30 years, e.g. 20-25 years for a wind turbine [3], and 10 years on average for recreational boats and vehicle bodies [4]. End-of-life (EoL) CFRP waste management is becoming increasingly important due to the rapidly developing demand for composites in industrial manufacturing. Nowadays, landfilling is still the most common waste management technique, which is reasonably inexpensive,

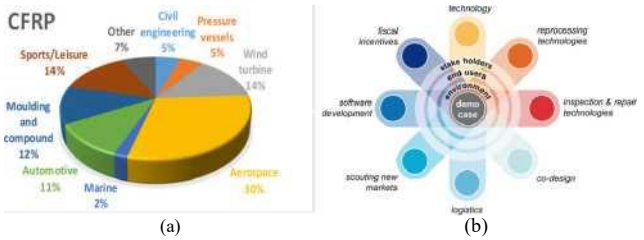

(a) (b)

Fig. 1. (a) CFRP-based products in different industries, (b) technical coverage of FibreEUse, source: http://fibreeuse.eu/

however it does not meet the rules in the Waste Framework Directive (2008/98/EC) and is not the most efficient way to dispose of EoL composites. Furthermore, its cost is expected to rise as a result of regulations in the future. A number of EU nations, e.g. Germany and Austria, have already banned the landfill of composite trash, which will be the trend in the future.

Remanufacturing and reusing are the best solution to EoL composites, which complies with the environmental regulations as well as benefits the stakeholders. However, it has been hindered by a number of factors, including a bad perception of recycled goods, inferior business models and recycling procedures, a lack of synergistic using inspection, repairing, and remaking technologies. The EU H2020 project FibreEUse is funded to solve these issues by integrating innovative recycling, remanufacturing, inspection technologies, and profitable reuse options for EoL composites (Fig. 1(b)).

During the remanufacturing process, the EoL products will be disjointed into individual components (Fig. 2), which are then refurbished and reused in new products afterwards. To make a better decision of refurbishing tactics and reuse alternatives, non-destructive testing is very critical since it provides a reliable and efficient assessment of the health conditions of the composites in the remanufacturing chain.

Visual inspection, ultrasonic testing, guided wave testing and thermal imaging are the most popular non-intrusive inspection methods for composite materials [5]. Since no extra non-destructive testing (NDT) tools are required and optical wavelengths are suitable for the human eyes, visual inspection is considered as is a quick and low-cost inspection approach. However, compared to an instrumented inspection, this method

This work was supported in part by the EU H2020 grant 730323 (FibreEUse).
Corresponding author: Prof. J. Ren (e-mail: jinchang.ren@ieee.org).
Y. Yan and J. Ren are with National Subsea Centre, Robert Gordon University, Aberdeen, U.K.
H. Zhao and J. F.C. Windmill are with the Dept. of Electronic and Electrical Engineering, University of Strathclyde, Glasgow, U.K.
W. Ijomah is with Dept. Design, Manufact. & Engineering Management, University of Strathclyde, Glasgow, U.K.
Jesper de Wit is with INVENT GmbH, Christian-Pommer-StraBe 47,38112 Braunschweig, Germany
Justus von Freeden is with Fraunhofer Institute for Machine Tools and Forming Technology IWU, Hermann-Munch-Str. 1, 38440 Wolfsburg, Germany

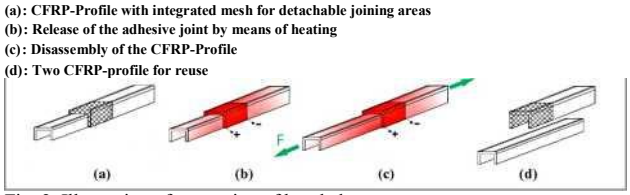

Fig. 2. Illustration of separation of bonded parts.

is labour intensive and unreliable for detecting microscopic flaws. As a solution to these issues, a Red (R), Green (G), and Blue (B) based RGB colour camera was utilised for improved damage detection and fault localization [6]. However, weather and lighting conditions might still have an impact on its effectiveness [7]. Ultrasonic testing can detect the internal flaws by analysing the sending and the receiving pulsed echo between one and/or multiple transducer(s). It is an efficient and safe technique, but it sometimes suffers in dealing with non-smooth and complex geometry surfaces, pretentious to subjective and objective factors [8]. Guided wave testing is a type of ultrasonic testing in which the wave propagation is guided by the boundaries of the object to be tested. Depending on the boundary conditions, different guided wave models can be obtained. Generally, lamb wave is widely used for condition monitoring as it has a good behaviour for thin plate-like structures [9], which is suitable for identifying both external and internal damages and condition assessment in various structures [10]. However, lamb wave has limited applications in the composite structures as its attenuation is very fast in the composite structures, leading to reduced sensing areas. In addition, its real-world application is also limited by not only the complexity, dispersive and multi-path characteristics, but also temperature variation caused instability [11]. Thermal imaging is a thermoelastic effect based inspection technique, where defects in the testing region is expected to present a higher temperature response [12]. This technique requires sensitive and expensive instrumentation, and highly skilled technician to run the instruments [5]. Moreover, the conduction and convection processes may also affect the temperature variations, leading to a barrier to localise the inspection [13]. In general, most of these techniques extract information about the physical integrity of the structures rather than the material composition from the objects. In this context, HSI can provide a novel insight to fill this gap. HSI is an emerging technology that combines imaging with spectroscopy, allowing for the acquisition of both spatial data as well as spectral data spanning wide frequency range. Thus, it can detect minute variations in temperature, moisture and chemical composition. It will also not be limited by environmental temperature and geometry of the object, making it a unique solution for non-destructive inspection far beyond conventional techniques [14].

HSI has been successfully applied in the field of food and drinks inspection [15], land mapping [16, 17], biomedical diagnosis [18, 19], and atmospheric sciences [20], etc. Recently, HSI has been increasingly applied for non-destructive inspection of composite structures in the industrial applications. In [21], visible and near-infrared spectral data were used to analyse the mechanical properties of wood fibre composites for quality control during polymer processing. In [22], NIR HSI was employed to estimate the resin thickness for structural health assessment of the aerospace grade carbon fibre composite. In [23], NIR spectrum was used for impurity detection of the plastic materials. In [24], NIR diffuse reflection spectroscopy was used to grade the chemical structure of the polymer composite by evaluating the concentration of the substances from absorption and determining the size and dispersity of filler from scattering. In [8], visible and NIR spectrum was used to detect surface defects including erosion and scratches on the wind turbines. Although a certain degree of success was reported, there is a lack of a systematic framework for HSI based non-destructive inspection, where relevant applications in (re)manufacturing are still rare. As an emerging application, applying HSI for non-destructive inspection on fibre composites in the remanufacturing chain is presented in this paper, where three case studies are detailed, including adhesives residual detection, surface damage detection, and robot integrated industrial inspection.

FRP products usually comprise FRP components or a combination of CFRP and metal components via adhesive bonding. For reuse purpose, these EoL FRP products need be disassembled with the adhesive bond being separated. However, adhesive residues will still adhere to the surface of the components and structures, which will be cleaned by laser treatment whilst the surface will be refurbished before the next bond. Although laser treatment has the potential advantage to clean the remnants adhesive, it has the risk of thermally degradation of the joint section. To monitor the surface condition such as the residual adhesive, and grinding defect caused during the laser treatment in real time, an NDT method is highly needed. To tackle this issue, HSI will be introduced, and its usefulness will be demonstrated as our first case study.

After the process of adhesive removal, the condition of each EoL component is decisive for their reuse. Components with irreparable damages cannot be reused and thus need to be recycled by thermal or mechanical processes. Components with minor damages can be repaired. For other undamaged components, surface treatments or coating can be applied to increase the perceived quality. Therefore, it is important to evaluate the damage cases of these components, which can help to determine the correct repair or refurbish strategies in order to maintain the structure integrity. This will form our second case study, where HSI and computer vision will be used for surface damage detection and assessment.

In the (re)manufacturing process, robotic systems become more and more widely adopted for industrial automation. For the industrial deployment of the HSI camera, an automatic HSI inspection system with human-robot interaction is proposed and trialled as our third case study. This system is integrated by a HSI camera and an industrial robotic manipulator, i.e., the KUKA KR06 R900, where the long arm of the robot can enable inspection of large-scale components to satisfy industrial needs.

The main contributions of this paper are highlighted below.

1) We propose a multidisciplinary systematic framework for fast, accurate and non-destructive HSI based inspection, which is essential for condition assessment, quality control and repurposing of CFRP in the (re)manufacturing applications.

2) An extendable cobot platform is developed for automatic NDT of size-independent materials, where multiple

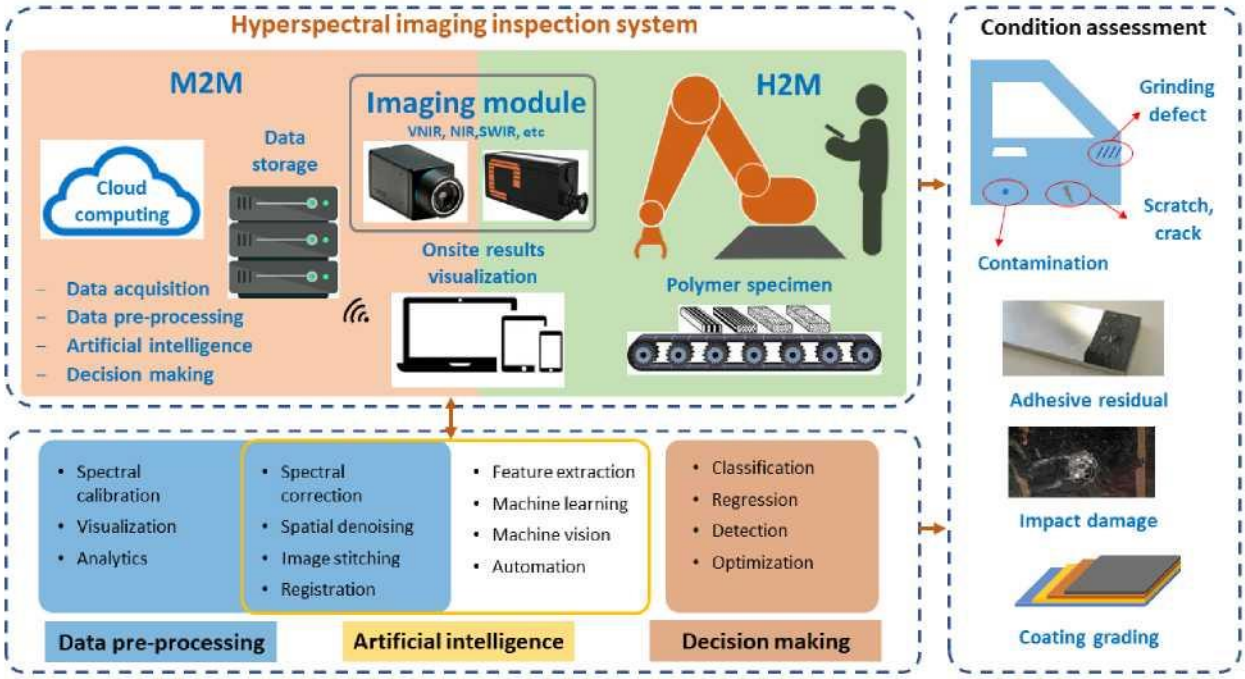

Fig. 3. Hyperspectral imaging inspection system for condition assessment in manufacturing and remanufacturing sectors, where M2M and H2M denote Machine-to-Machine and Human-to-Machine interactions, respectively.

disciplines are introduced including HSI, robotics, data pre-processing, artificial intelligence and decision making, etc.

3) We have carried out three case studies to validate the feasibility and effectiveness of the HSI based inspection system in the automotive remanufacturing chain, where useful discussions and conclusions were reported.

The remaining paper is organised as follows. Section II describes the concept of the HSI based inspection system. Section III discusses the way to data acquisition and data processing in this system. Section IV details the three case studies. Finally, Section V summarises some concluding remarks and future directions.

II. Hyperspectral imaging inspection system

Fig. 3 depicts the concept of the hyperspectral imaging inspection system for the (re)manufacture industry, which is composed of three core modules, i.e. Imaging module, Machine-to-Machine (M2M) interaction Module, and Human- to-Machine (H2M) collaboration module. In the Imaging module, the optical sensors such as visible (VIS), near-infrared (NIR), and short-wave infrared (SWIR) hyperspectral cameras can provide a continuous spectral information over a certain spectral range, along with a good spatial resolution. M2M can actually provide a continuous information flow between the imaging devices and computer vision algorithms for data processing and analysis. Hereby, the sensors, onsite data acquisition machine, offsite data storage devices and cloud data processing units can connect and communicate to each other via the industrial IoT (mostly based on wireless network). In addition, H2M collaboration is also a very important module. Here, human workers, hyperspectral cameras and the specifically designed compliant robots can work together in carrying out complex and unstructured inspection tasks at the remanufacturing and repair production lines.

Within the M2M techniques, data processing is considered as the enabling technology and covers three streams, i.e., data pre-processing, artificial intelligence (AI) and smart decision making. Data pre-processing is a vital step after data acquisition for data calibration and enhancement, which can produce high quality data for easy understanding and improved analysis via data visualization and analytics. According to the practical needs of different NDT tasks, data pre-processing sometimes needs to be incorporated into AI, where spectral correction and spatial denoising techniques are needed for improving the data quality, as well as image stitching and registration techniques for data fusion and full-scale representation.

The main AI techniques include but not limited to feature extraction, machine learning, computer vision and automation, etc. One of the biggest issues with analysing hyperspectral data is the large number of variables involved, leading to the curse of dimensionality. A high number of variables necessitates a considerable number of samples thus the corresponding memory and processing capacity, and it may also lead to overfitting of the classifiers when training the model. To address this issue, feature extraction is needed for dimension reduction and more effectively characterisation of the data.

Machine learning algorithms have been widely applied in numerous industrial applications, which are usually built upon the sample data (also known as training data) before being applied for prediction or decision making. The purpose of automation is to implement the monotonous tasks e.g. data acquisition by machines (i.e., KUKA robots), to reduce human intervention and improve the efficiency and productivity.

Computer vision can be considered as an integration of feature extraction, machine learning and automation, which can provide imaging-based automatic inspection, big data process control and robotic implementation. The outcomes of these techniques are eventually used for decision making such as

classification, regression, detection and optimization. The proposed hyperspectral imaging inspection system can be employed for generic condition monitoring and asset management for the repair and remanufacturing of CFRP materials. Relevant applications can be found in the detection of defects such as contamination, scratch, and grinding defect, recognition of adhesive residual, classification of impact damage types, and quality grading of coating.

III. Techniques and Methodologies

In this section, the standard progress of data acquisition in the lab environment and data pre-processing techniques are introduced. Those techniques are not only used in this work but also applicable in many other HSI applications.

A. *Data acquisition*

In our three case studies, the hyperspectral data is acquired by two hyperspectral systems, where a visible (VIS) hyperspectral system is used for surface damage detection and a near-infrared (NIR) hyperspectral system for residual adhesive detection. Both systems can be incorporated into the robotic platform for H2M collaborations.

Both hyperspectral systems function in the push-broom mode, where the camera's lens is facing down and only one line is scanned at a time. Two 20 W Tungsten halogen lights are used for illumination. Each scan produces a two-dimensional image in which one dimension represents the spatial line and the other dimension represents the complete spectrum of each pixel. For the first two case studies, the samples to be scanned are moved using a translational stage at a consistent speed of 16mm/s with a working distance of 25 cm beneath the camera, to form the 3D hypercube data. For the last case study, the translational stage is replaced by the KUKA robot arm, and the implementation detail will be discussed in Section 4.3.

The VIS imaging system is comprised of a Hamamatsu ORCA-03G CCD camera and a Specim V8E spectrograph. This system operates in the spectral range of 400-950 nm and has a spectral resolution of 2nm. In addition, 4-fold spatial and spectral binning were applied in order to minimise noise and boost the camera's light sensitivity. This also results in an image with 336 pixels per line and 256 spectral responses per pixel.

The NIR imaging system is Innospec Red Eye 1.7. It operates in the spectral range of 950-1700 nm with a spectral resolution of 10 nm. The number of spectral bands and spatial pixels per line without binning is 256 and 320, respectively.

B. *Data pre-processing*

1) *Spectral calibration*

During the data acquisition stage, the lighting conditions may shift within a hypercube or apparently between different datasets along the scan lines. To mitigate the effect of camera quantum and physical configuration differences on imaging systems, reliable calibrations for the HSI system are required to ensure the stability and acceptance of the hyperspectral data produced. As a result, light calibration is required to convert the raw radiance spectrum s to the reflectance spectrum r in order to reduce this incoherence and retain a consistent influence of the light conditions. Without exposing the camera to light, we may get a dark reference spectrum d. Then a white reference spectrum w can be obtained by imaging an ideally reflective white surface (e.g., Spectralon with Lambertian scattering). The present illumination's light sensitivity may be calculated by normalising the signal by:

(1)

2) *Spectral correction*

As the retrieved spectra are dependent on both chemical absorption and physical light scattering, according to the objects' surface structure. After spectral calibration, spectral correction is required to convert the spectra to the Standard Normal Variate (SNV) [25] in order to minimise scattering errors. For any pixel with a reflectance spectrum r_s in the HSI $D \in {}^{I \wedge X x Y x B}$ at (1,7) where $i \in 1{:}X, j \in 1{:}Y$, the process of SNV is defined by Eqs. (2-5), where $D(i,j,b_{1:B})$ represents a spectral vector with a length of B at location (i,j); p and a denote the mean and standard deviation of all pixels in r_s.

$$r_s = D(i,j,b_{1:B}) \tag{2}$$

$$r_s(W) = \wedge\wedge \tag{3}$$

$$\mu = \frac{1}{I \times J} \sum_{s=1}^{I*J} r_s \tag{4}$$

$$\sigma = \sqrt{\frac{1}{I \times J} \sum_{s=1}^{I*J} (r_s - \mu)^2} \tag{5}$$

3) *Spatial denoising*

Apart from the spectral degradation, the acquired data can also be degraded by instrumental noises such as thermal noise, quantisation noise and shot noise in the spatial domain. As a result, spatial denoising is needed to mitigate the noise. Herein, the bilateral filtering as a nonlinear approach that allows edge-preserved noise removal is employed. For a 3D hypercube, spatial smoothing is accomplished using an enhanced joint bilateral filtering (JBF) [26]. Given a HSI data $D \in {}^{XxYxB}$, X and Y represent the spatial dimensions of D and B represents the number of spectral bands. The JBF result for the input data D at the location (i,j) of band b can be derived as follows:

$$D_{JBF}(i,j,b) = \wedge\text{—} \wedge^{J}_{(p,q)\in w} (G_{ad}(i-p,j-q)\, x\, G_{,,r}(W(i,j) - Ipci(p,q))D(p,q,b)) \tag{6}$$

where the local window w that is centred on (ij) has a size of $(2a_d + 1)$ x $(2ct_r + 1)$ pixels.

The normalisation factor k is defined by

$$Hi\cdot j) = \wedge^{(p,q)\in w} (G\wedge ii-pJ-q)\, {}^{x}G<r_r(p_{PCI}(i,f) — D_{PCI}(p,q))\wedge \tag{7}$$

where the first principal component D_{PCI} is derived from the principal component analysis (PCA), and (p,q) signifies a pixel's spatial position inside w.

The kernels for domain and range filtering are given by:

$$Ga_d(i-p,j-q) = exp[-\blacksquare \frac{(t-p)^2 + (/-q)^2|}{2 \circ l} \tag{8}$$
(8)

$$Ga_r\{p_P ci(.i,]) D_{PC1}(p,q))$$
$$\_ \quad ((Dpci(j,D - Dpc_i\_(p,q)')^{\wedge} \quad (9)$$
$$\sim^{eXP}\{ \quad 2^{\wedge})$$

where a_d and a_r represent respectively the domain and range parameters, and decide the edge-preserving performance [27].

IV. Case studies and discussions

In this section, three case studies are presented to show the potential of proposed HSI based NDT of fibre materials, including specific AI techniques introduced in the context.

A. *Case study 1: Adhesive's residues detection*

1) *Experimental materials*

In the first study, three samples are used, which are single Aluminium (Al), adhesive bonded CFRP-CFRP and adhesive bonded CFRP-AI tensile shear samples (Table 1). CFRP composites are fabricated from automotive grade continuous fibre reinforced epoxy resin with the carbon fibres.

2) *Experimental results*

After data acquisition, two pre-processing steps are carried out, which include spectral calibration (Eq. (1)) and spectral correction (Eqs. (2-5)). To visualise the spectral characteristics of the surface conditions of the three samples, an image at the wavelength of 1267 nm is shown in Fig. 4, where the average spectral profiles over the whole bands of the selected regions of interest (ROI) are also platted for comparison in Fig. 4(a-c). To visualize the differences further effectively between regions of interest, we applied the PCA to the calibrated data and showed the first three extracted PCA components in Fig. 4(d-f). We have also demonstrated the feature space of different regions on the PCA domain using the t-SNE method [28] in Fig. 4(g-i).

For the Al sample, three regions, i.e., normal region, grinding region and grinding defect region, are compared with different spectrums. These regions are manually extracted according to the knowledge from domain expert and sample provider in INVENT-GmbH. For the normal region, the intensity is low as the surface is furbished and has a relatively lower reflectance. The lowest intensity on its normalised reflectance can be found between 1333 nm and 1600 nm. For the grinding region, it has high reflectivity, which leads to high reflectance and appears white on the colour image. Its normalised reflectance has the highest intensity between 1333 nm and 1600 nm, with a standard deviation lower than that of the other two regions in the range of 996-1333 nm. Due to poor laser treatment, some defects are caused in the grinding region. The defect region has a lower reflectivity than the other

Table 1 Illustration of tensile shear samples and their dimension information.

Material	Samples	Thickness (mm)
Al	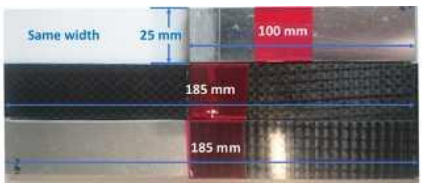	3.22
CFRP+CFRP		4.48
CFRP + Al		5.60

grinding region, which looks grey on the colour image. Its normalised reflectance is in between of other two regions in the spectral range of 1333- 1600 nm. Although its profile has the similar trend to the normal region within 996-1333 nm, there are still some gaps between the two spectra, which shows their difference. As seen from the first three PCA components, although the clusters of the three regions are somehow distinguishable, the clusters of grinding region and grinding defects are still quite close to each other (Fig. 4(d)). After mapping the extracted features from the PCA domain to the t-SNE space (Fig. 4(g)), the features extracted from different regions are found to be more discriminative.

For the CFRP+AL sample, four representative regions are highlighted in differently coloured boxes on the colour image (Fig. 4(b)). The blue and yellow boxes denote the normal region and the adhesive region on the Al side, respectively. The red and purple boxes are the normal region and the adhesive region on the CFRP side, respectively. In the colour image, it can hardly recognise the adhesive residual on the materials. However, apparent difference between the normal region and the adhesive region can be seen on the spectral profile. As seen in Fig. 4(b), the wavelength 1147 nm is an important turning point: the Al-normal region (blue line) has a lower reflectance before 1147 nm but higher reflectance afterward than the Al- adhesive region (yellow line). On the contrary, opposite reflectance trends of the CFRP- normal region (red line) and the CFRP-adhesive region (purple line) are shown. In addition, the spectral profile of the Al-normal region (blue line) and the CFRP normal region (red line) can be well distinguished. The Al-adhesive region and the CFRP-adhesive region have similar spectral reflectance throughout the whole wavelength. From the first three PCA components, it can be clearly seen that the clusters of the four regions of interest are separable from each other (Fig. 4(e)). For the normal region of AL and CFRP, the variance of the cluster is insignificant as the surface condition of each raw material shows high consistency. For the adhesive region, the variance of the cluster becomes larger and an overlapping issue appears, which is mainly due to the spectral mixture of the adhesive and the raw materials. As seen in the t- SNE feature space (Fig. 4(h)), the extracted features of each region of interest tend to be grouped into separate clusters, indicating the high discriminability of the features.

For the CFRP+CFRP sample, Fig. 4(c) presents four spectral profiles of two pairs of CFRP samples, which include two adhesive regions (yellow and purple boxes) and two normal regions (red and blue boxes). As can be seen, in each pair of samples, the spectral profiles show a high degree of similarity. However, the spectral profiles from the two pairs are much different, which indicate the inter-class dissimilarity between the normal and adhesive regions. In Fig. 4(f), two clusters of the normal regions and two clusters of adhesive regions are shown at different locations in the first three PCA components' domain, though their boundaries are not clear in between.

However, the discrimination between normal and adhesive regions are successfully separated in the t-SNE feature space (Fig. 4(i)) where two manifolds of the normal regions overlap with each other but clearly differ from two manifolds of the adhesive regions. Thus, HSI is tested for distinguishing the adhesive residual in this study, which can benefit the laser

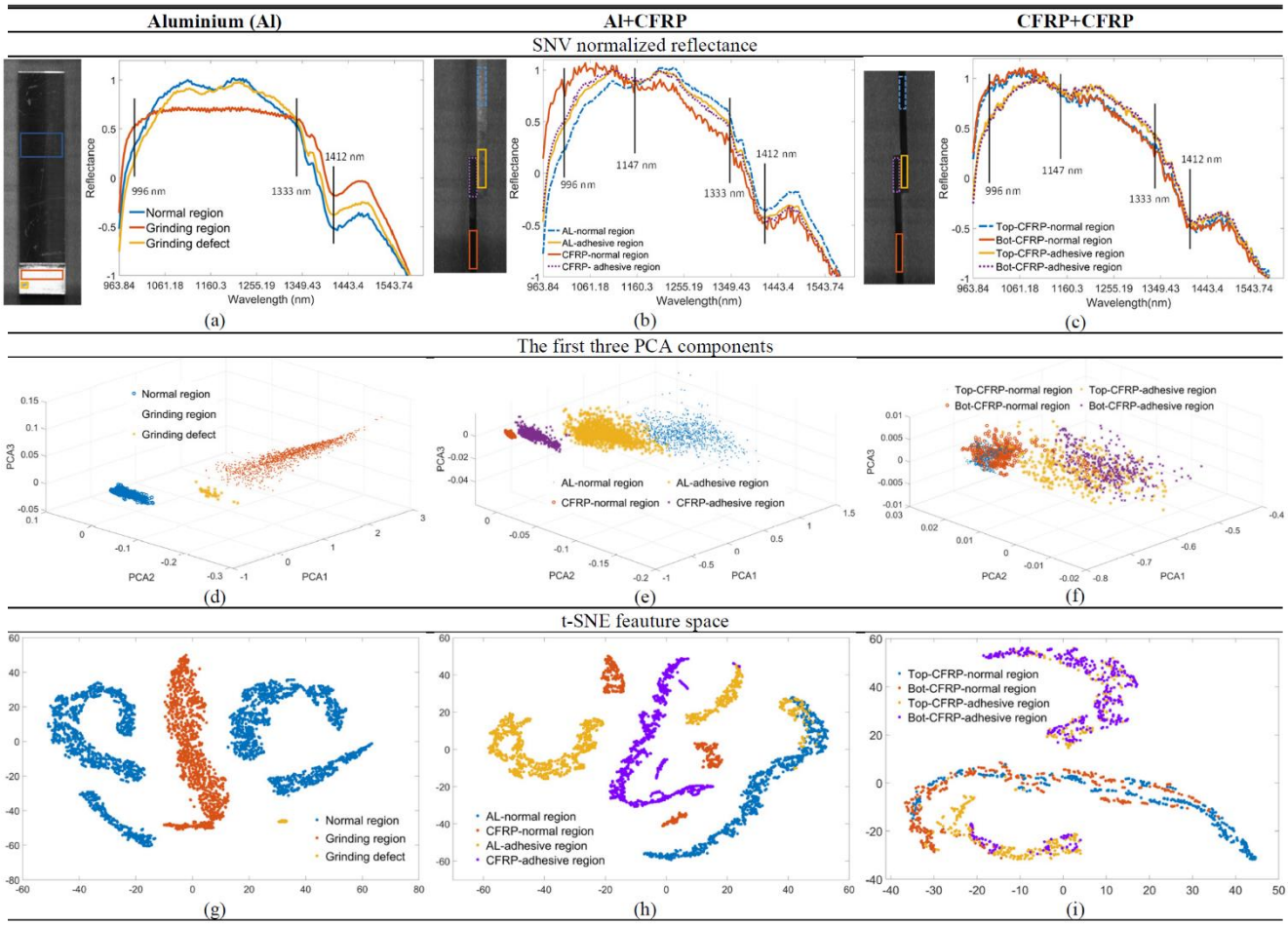

Fig. 4. SNV normalized spectra (To the left are the colour images and to the right are the averaged spectrums from selected ROIs.), first three PCA components and t-SNE feature space of different regions on the Al (a,d,g), CFRP+Al (b,e,h), and CFRP+CFRP (c,f,i).

treatment during the disassembly stage and provide useful information for the grading of adhesive cleaning and other surface conditions. Last but not the least, all these results have clearly validated the following findings:

1) Pre-processing and feature extraction are found extremely useful for spectral data analysis, which will benefit the efficacy and accuracy of the HSI inspection system.
2) HSI is able to differ the furbished (normal) region, grinding region and grinding defect region.
3) HSI is able to identify and detect the adhesive residual.

B. *Case study 2: Surface damage detection*

1) *Experimental materials*

In the second study, three kinds of CFRP specimens, manufactured by Resin Transfer Moulding (RTM) and Bulk Moulding Compound (BMC), were intentionally damaged by two types of impactors, while all the experiments are repeated three times. In the RTM process, fibre preform is laid in a two-part, matched, closed mould, before the thermoset is injected into the closed mould under low to moderate pressure [29]. For the BMC process, it is usually done by applying pressure and heat to the mould where a bulky mixture of fibres, resin paste and fillers is placed [30]. In our experiment, the first sample is manufactured via RTM using endless carbon fibre textile and epoxy matrix. The second sample is produced via BMC using new carbon long fibres, i.e., 45% fibre content with 25 mm fibre length. The third sample is also manufactured by BMC using thermal recycled carbon long fibres i.e., 45% fibre content with 25mm fibre length. For a compact presentation, the three samples are denoted as RTM, BMC and RCY, respectively in the remaining paper. The experimental settings consist of a down pipe with a height of 2 meters. Each falling body has a weight of 607g, resulting in an impact energy of 11.9 joule. The impact test results from different settings are given in Fig. 5.

2) *Optimised data acquisition*

During the experiments, it is found that taking advantage of diffusion scattering and reflection of light can actually highlight the damaged regions even in the raw data. When the imaging camera vertically faces downwards the sample, the damaged region on the sample surface is hardly seen by the naked eyes. This is because the lights from two lamps form an even diffuse reflection on the surface of the sample when the image is acquired. Therefore, the camera may capture many unwanted textures on the surface, as shown in Table 2(b). By changing the placing angle between the sample and the movable stage, we can make the angle of incidence close to the angle of the reflection. This can bring in two benefits: 1) the camera can accurately record the light from lamp1 (Fig. 5(d)), and the

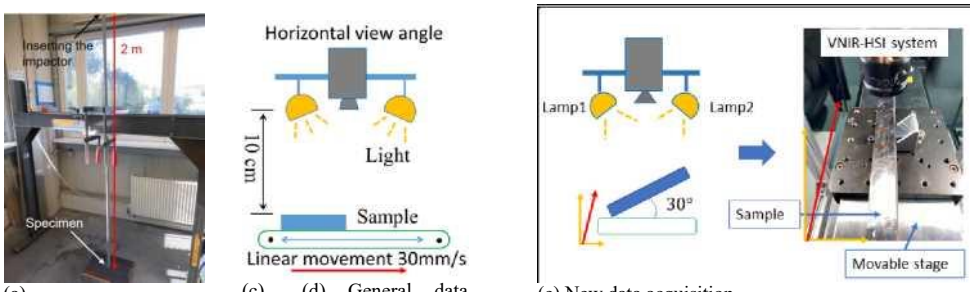

(a) (c) (d) General data acquisition (e) New data acquisition

Fig. 5. Illustration of impact test setting-up (a) for Painted body impactor (b), Wedge-shaped body impactor (c), generic data acquisition (d) and our new data acquisition (e) in the second case study.

Table 2 Visual comparison between phone captured data (a), general (b) and new (c) data acquisition manners.

	Point body impactor	Wedge-shape body impactor
(a)	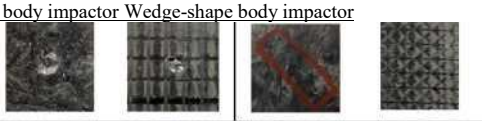	
(b)		
(c)		

surface can be captured in a good condition; 2) the diffusion scattering on the damaged region(s) can be enlarged so that the camera captures less light from those regions. On the other hand, lamp2 is also useful in this setting as it can further enlarge the diffusion scattering on the damaged region. Thus, the contrast between the damaged regions and the background can be enhanced in the captured data. Some damaged regions (Table 2(a)) that cannot be seen physically in conventional settings (Table 2(b)), now become clearly visible in the newly acquired data (Table 2(c)). The placing angle is dependent on the practical experimental settings, though we use 30° in our experiments. Afterwards, the acquired data will be translated back into the normal dimension by the cosine law. Some visual results are shown in Table 2 to illustrate how this process works.

3) *Damage detection framework*

Accurate distinguishing the types of damage is always of interest for determining the suitable repairing strategy for the damaged fibre composites. As such, an integrated HSI based damage detection system with machine learning and computer vision technologies is proposed. This is a multi-stage image processing framework (Fig. 6) that is composed of three key modules, i.e., pre-processing, saliency detection and feature output. It can detect the damaged regions and calculate the roundness *(Rd)* and rate of the major axis vs. the minor axis *(RMM),* see in Eqs. (10-11), as detailed below.

After data acquisition, two pre-processing steps are carried out, which include spectral calibration and spatial denoising, following the same procedure defined in Eq. (1) and Eqs. (6-9), respectively. Afterwards, ROI extraction is implemented from the first principal component of the hypercube through a saliency detection module [31] for generating a gray-scale saliency map of the damaged regions. In the feature extraction

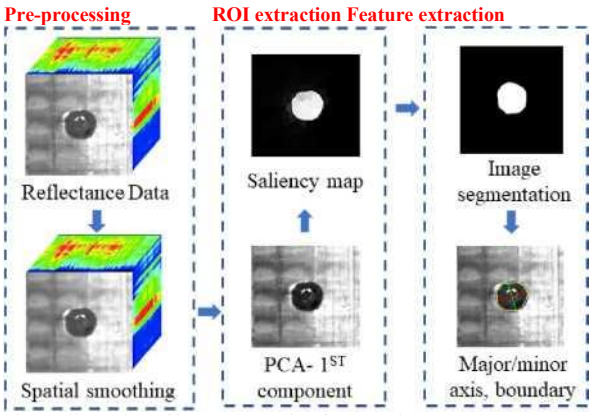

Fig. 6. Illustration of image processing framework.

step, a hard threshold is applied to convert the saliency map to a binary image, where the ROI will be highlighted as white pixels with the background in black. The boundary of ROI can be approximated by an ellipse with the associated parameters determined, including the roundness (Eq.10), ratio of the major axis and the minor axis (Eq.11) that has the same normalised second central moments as the ROI, where a and p denote the area and perimeter of the ROI, respectively.

$$Rd = \frac{<!\bullet An}{p^{*}} \quad (10)$$

$$RMM = \frac{major\ axis}{minor\ axis} \quad (11)$$

4) *Experimental results*

To validate the usefulness of our damage detection system, we show examples of damage detection in Fig. 7, in which the colour images captured by a phone camera presented in columns (a) and (e) for visual comparison. The ground truth annotated by the domain experts are shown in columns (b) and (f). The damage detection results from the acquired HSI image are given in columns (c) and (g). The extracted features are illustrated on the HSI acquired data in columns (d) and (h), with the boundaries highlighted in yellow, the ellipse of the ROI shown in blue, and the major axis and the minor axis illustrated in red and green, respectively. In addition, the damage regions caused by the point body impactor and the wedge-shaped body impactor on the three materials are highlighted by red circles and red rectangles, respectively.

As shown in Fig. 7(a) and Fig. 7(e), the point body impactor causes a round-shape surface sag, and the wedge-shaped body impactor causes two bar-shape surface sag on the three

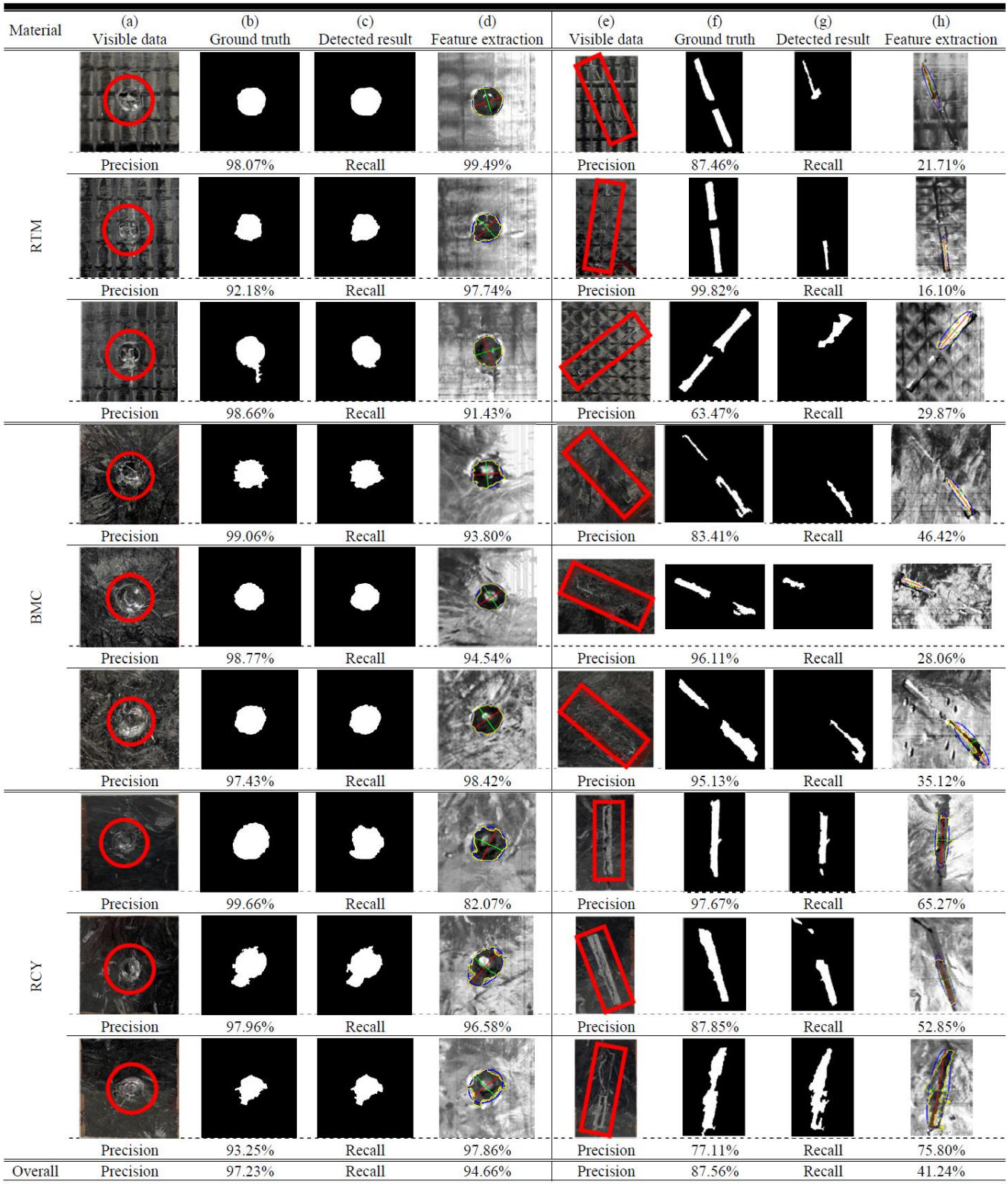

Fig. 7. Results of damage detection: Damages (in red circle) caused by pointed body impactor (a) and (e), their ground truth maps (b) and (f), the detected results (c) and (g), and the corresponding features (d) and (h).

materials. The bar-shape damage is hardly seen on the surface materials. As a result, the stiffness of RTM and BMC is higher of RTM and BMC samples but is clear shown on the surface of than that of RCY. Another finding from Fig. 7 is that the RCY. This is because RTM and BMC are manufactured by damage region appears more clearly in the HSI than in the original fibres, but RCY is manufactured by recycled BMC colour image from the phone camera, especially for the defects

on the RTM and BMC materials. This has validated the efficacy of HSI than colour imaging.

For quantitative evaluation, pixel-level precision and recall values are used to evaluate the damage detection results:

$$Precision = \frac{Tp}{Tp + Fp} \quad (12)$$

$$Recall = \frac{Tp}{Tp + Fn} \quad (13)$$

where *Tp*, *Fp*, and *Fn* denote respectively the number of properly identified foreground pixels in the damage zone, the number of wrongly detected foreground pixels (false alarms), and the number of missing pixels from the damage region [32].

In the developed image processing framework, damages caused by the pointed body impactor can always be detected, with the precision and recall values over 90% (sometimes ~100%) in most cases. Nevertheless, it still has difficulty to detect damages caused by the wedge-shaped body as a whole on the surface of all materials. There are two main reasons: 1) the limited impact energy of 11.9 joule is not strong enough to make visible damages on the surface, 2) the complex nature of the surface texture has made the surface damage hardly visible. As a result, although the average detection precisions for BMC, RTM and RCY can reach 91.55%, 83.58% and 87.54%, the average recall values are only 36.53%, 22.56% and 64.64%, respectively. As seen in Fig. 7(d), the damages on the RCY are often quite fully detectable because the recycled BMC material has a lower stiffness, making it more vulnerable to the impact and resulting in more visible surface damages. Therefore, its recall value is much higher than BMC and RTM.

Finally, the overall precision and recall measures for the two kinds of damages are obtained by the weighted average of all samples. For the pointed body damage and the wedge-shape body damage, the overall precision values on the three materials are 97.23% and 87.56%, respectively, with the overall recall values becoming 94.66% and 41.24%. Again, a high precision with a low recall value indicates that the HSI based integrated solution has a high reliability of positioning the impact damage. However, it fails to detect the whole damaged region, especially for the wedge-shape body or complicated geometric damages.

After damage detection, the representative features of the damage regions i.e., roundness and the RMM are extracted and plotted in Fig. 8 for comparison. With satisfied measures of the precision and recall, the RMM values for point body damage are consistently close to 1. The roundness varies from 0.65 to 1,

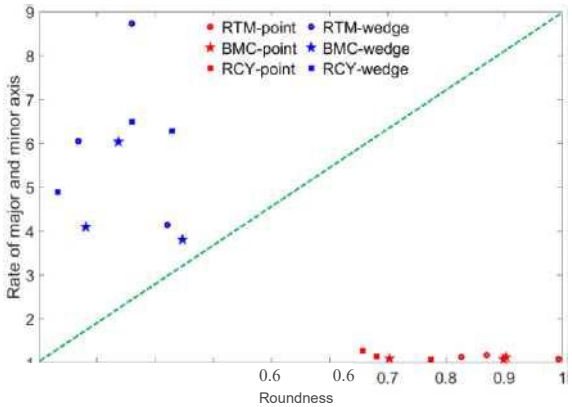

Fig. 8. Scatter plot of damage features.

as the shape formed by the damaged region is not always round. For the wedge-shape body damages, with a high precision and a low recall, both the RMM and roundness have large variance, i.e. RMM £ [3.8,8.8] and roundness £ [0.13,0.35]. However, the features of these two damages are still easily distinguishable, which validates again the efficacy of HSI in NDT of the fibre material, and its potential for facilitating smart decision-making of requested repairing strategies.

C. *Case study 3: Cobot based automatic inspection*

1) *Experimental materials*

In the third study, a large automotive body structure sample that is made of UD-fibre (0°), biaxial fabric (0°/90°, -45°/45°) and a unsaturated polyester resin is damaged by a sharp impactor and a round impactor (Fig. 9). The experimental setup consists of a down tube with a height of 5.6 meters. The falling body has a mass of 2 kg, which results in an impact energy of 109.8 joule. As seen in Fig. 9(d), the damage caused by the sharp impactor is noticeable, but the damage caused by round impactor is almost invisible.

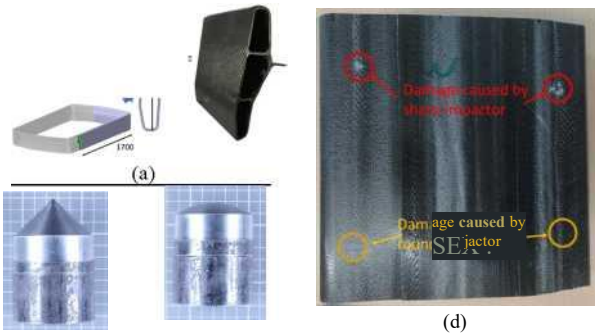

Fig. 9. Illustration of the body structure (a), sharp impactor (b), round

2) *Experimental equipment*

In addition to the two HSI cameras, a robotic manipulator, the KR06 R900 [33] from KUKA is used in this case study, mainly for its universality in many industrial applications. The robot is a 6-axis serial manipulator, with characteristics and working envelop shown in Fig. 10(a).The real setting in the lab environment is shown in Fig. 10(b), where the large automotive body structure is fixed to a holder mounted on the robot. The working distance between the camera and the sample surface is 25 cm. The movement of the robot is manipulated by an accompanying controller. During the camera scanning, the robot will drag the sample moving along Axis2 with a speed of 16 *mm/s*. A laptop will record the hyperspectral data into the 'ENVI' format. The proposed system can also be implemented

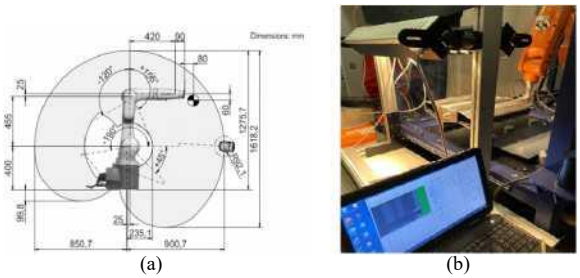

Fig. 10. Cobot system in the lab environment, (a) working envelope with dimensions comprised during operation for KUKA KR06 R900, (b) laboratorial cobot workplace.

with any other serial manipulators such as Asea Brown Boveri (ABB) [34] and Staubli [35].

3) *Image stitching*

Due to the limitation of the field of view, each scan can only cover a spatial dimension of 15 cm. As the width of the car body sample is 28 cm, dual scanning is needed to cover the whole surface. To represent the sample surface as a whole, a simple image stitching method is used in this study. Let the spatial dimension of scanned HSI data be $x * y$. The spatial dimension of the overall surface will be $(2x - Ax) * y$. In this study, x is decided by the spatial size of the HSI camera, i.e. 320 pixels; and y is decided by the scanning path, or 620 pixels in total. Ax is manually decided as 110 pixels in this study. To this end, the dimension of sample surface turns to be 530*620 pixels.

4) *Experimental results*

For visualisation purpose, image stitching is first applied to each HSI band, before conducting the PCA on the hypercube to extract the most representative features from the data. The 1st PCA component is shown in Fig. 11.

In Fig. 11(a), regions 1 and 2 highlight damages caused by sharp impactor, and regions 3 and 4 highlight damages caused by round impactor. In Fig. 11(b), regions 1-4 are the corresponding healthy regions in Fig. 11(a). For the sharp impactor, it can break the fibre into the contacted region and deform the fibre in the surrounding regions. Therefore, it will make the damaged surface more sensitive to the light and produce higher reflectance. As seen in Fig. 11, compared with healthy regions, impactor-contacted regions show a bright colour, with many white dots formed on deformed regions in the PCA domain. For round impactor, it won't break the fibre but will deform it in a larger area. As a result, there are only sparse white dots showing in the PCA domain.

To further highlight the difference between the damaged regions and healthy regions. We present averaged spectral profile for those regions in Fig. 11(e-h), where the standard deviation (std) is also plotted using shaded area. As the impactor will break and/or deform the fibre and change the reflectance of the neighbouring areas, both the reflectance and spectral standard deviation of the damaged regions are always higher than those of the healthy regions. By further suppressing the intensity of the background pixels, we can enhance the features in the PCA domain. As shown in Fig. 11, the pixel intensity in the healthy regions (Fig. 11(d)) appears darker than the damaged regions (Fig. 11(c)) after the background suppression. On a different note, the damaged regions show bright colour on the feature map, which indicates obvious defects on the sample surface, again validates the efficacy of HSI in NDT of CFRP materials.

V. Conclusions and Future Work

In this paper, novel insights are provided into HSI enabled non-destructive testing of CFRP materials, using three case studies on different kinds of CFRP materials. All the artificially introduced damages and failures follow the European standards. In the first case study, the adhesive residual shows a remarkable difference against the CFRP and aluminium materials on the spectral signature. In the second study, the combination of the HSI and computer vision techniques is able to well detect two types of surface damages on the CFRP materials. In the third case study, a human-robot collaboration platform is developed, where the HSI camera and robot arm are integrated together for automatic NDT. The major advantage of this platform is that it is a generic one independent on any specified HSI sensors or robots. The case studies have fully validated its usefulness, efficacy and great potential of HSI in NDT of CRFP and beyond.

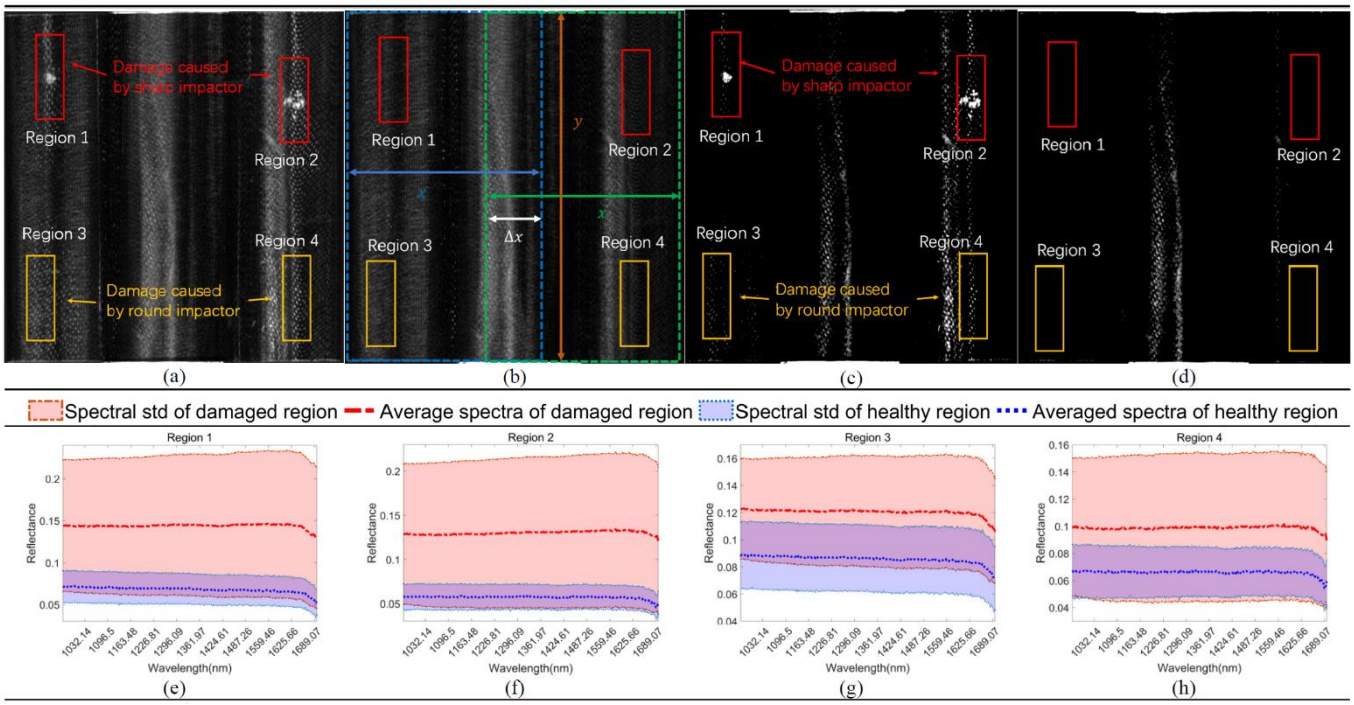

Fig. 11. Visualized 1st PCA component of sample front surface with damage (a) and without damage (b), (c) and (d) are enhanced feature map of (a) and (b), respectively. Averaged spectral profile of region 1-4 is shown in (e-h), respectively.

In addition, the proposed measurement technique can also bring the benefits to economy in the following aspects:

1) To support the sustainable transition of the industry to a circular economy model with a dynamic and flexible structure and low investment costs for composites
2) To save the energy cost during the decomposition process with better defined conditions and materials' characteristics.
3) To enhance the profitability, close the loop of composite lifecycle, avoid massive waste flows of high residual performance materials and allow the EoL CFRP reuse thus to save raw materials and minimise CO2 emissions.
4) With better inspection method, more effective repair and repurpose decision can be made, which will reduce the uncertainty and the variability of EoL CFRP flows and to better manage SMEs' capacity and investments.
5) To meet the main EU directives of landfill and 2008/98/EC, leading to a dramatic cost saving from landfilling of wastes.

In our future work, we will keep improving these three case studies for increased technology readiness level (TRL). First, how the amount of adhesive residual affects the spectral profile will be investigated, where a regression model can be built to quantitatively measure the concentration of adhesive residual through the HSI data. Second, the complex background is still the main obstruction for surface damage detection. As seen in Fig. 7(h), the damage caused by the wedge-shaped body impactor cannot by fully detected. To solve this issue, some sophisticated background modelling methods [36] can be employed to eliminate the effect of the background for improved damage detection. Third, for the cobot system, we will design more tasks to test its flexibility and liability via in situ experiments. Apart from these studies, we will also explore new NDT tasks for improved adaptiveness and completeness to meet the ever-changing market requirements.

On a different note, there are still some challenges and limitations. First, it cannot fully detect the inner damage such as delamination and void. This limitation can be mitigated by integrating other NDT techniques such as ultrasonic testing and thermography. Second, the push-bloom style of imaging is time consuming, which will be a barrier to the practical application. This can be solved by using snapshot HSI cameras such as Cubert [37] and Specim [38], etc.

References

[1] Y. Yan, et al, "FiberEUse: A Funded Project Towards the Reuse of the End-of-Life Fiber Reinforced Composites with Nondestructive Inspection," in *Int. Conf. in Commu., Signal Proc., and Systems,* Springer, pp. 1541-1547, 2019.

[2] M. Ramakrishnan, et al, "Overview of fiber optic sensor technologies for strain/temperature sensing applications in composite materials," *Sensors,* vol. 16, no. 1, p. 99, 2016.

[3] J. Beauson and P. Brandsted, "Wind turbine blades: an end of life perspective," in *MARE-WINT*: Springer, Cham, pp. 421-432, 2016.

[4] M. Onal and G. Ne^er, "End-of-life alternatives of glass reinforced polyester boat hulls compared by LCA," *Advanced Composites Letters,* vol. 27, no. 4, 2018.

[5] S. Gholizadeh, "A review of non-destructive testing methods of composite materials," *Procedia Structural Integrity,* vol. 1, pp. 50-57, 2016.

[6] F. P. G. Marquez and A. M. P. Chacon, "A review of non-destructive testing on wind turbines blades," *Renewable Energy,* vol. 161, pp. 998-1010, 2020.

[7] R. Bossi and V. Giurgiutiu, "Nondestructive testing of damage in aerospace composites," in *Polymer composites in the aerospace industry:* Elsevier, pp. 413-448, 2015.

[8] P. Rizk, etc, "Defect detection using hyperspectral imaging rechnology on wind turbine blade," *Remote Sensing Appl.: Society and Environment,* p. 100522, 2021.

[9] M. Mitra and S. Gopalakrishnan, "Guided wave based structural health monitoring: A review," *Smart Materials and Structures,* vol. 25, no. 5, p. 053001, 2016.

[10] X. Qing, et al, "Piezoelectric transducer-based structural health monitoring for aircraft applications," *Sensors,* vol. 19, no. 3, p. 545, 2019.

[11] R. Gorgin, Y. Luo, and Z. Wu, "Environmental and operational conditions effects on Lamb wave based structural health monitoring systems: A review," *Ultrasonics,* vol. 105, p. 106114, 2020.

[12] M. Barus *et al.,* "NDT-based design of joint material for the detection of bonding defects by infrared thermography," *NDT & E Int.'l,* vol. 93, pp. 157-163, 2018.

[13] A. Tesauro, C. Pavese, and K. Branner, "Rotor blade online monitoring and fault diagnosis technology research," DTU Wind Energy, 2014.

[14] X. Li, et al, "Hyperspectral imaging and their applications in the nondestructive quality assessment of fruits and vegetables," in *Hyperspectral imaging in agriculture, food and environment:* IntechOpen, 2017.

[15] Y. Yan, et al, "Nondestructive phenolic compounds measurement and origin discrimination of peated barley malt using near-infrared hyperspectral imagery and machine learning," *IEEE Trans. on Instrumentation and Measurement,* vol. 70, pp. 1-15, 2021.

[16] H. Sun et al, "Superpixel based feature specific sparse representation for spectral-spatial classification of hyperspectral images," *Remote Sensing,* vol. 11, no. 5, p. 536, 2019.

[17] S. T. Seydi and M. Hasanlou, "A new structure for binary and multiple hyperspectral change detection based on spectral unmixing and convolutional neural network," *Measurement,* vol. 186, p. 110137, 2021.

[18] Q. Hao *et al.,* "Fusing multiple deep models for in vivo human brain hyperspectral image vlassification to identify glioblastoma tumor," *IEEE Trans. Instrum. and Me as.,* vol. 70, pp. 1-14, 2021.

[19] X. Wei, etc, "Medical hyperspectral image classification based on end-to-end fusion deep neural network," *IEEE Trans. Instrum. Meas.,* vol. 68, no. 11, pp. 4481-4492, 2019.

[20] L. Xi *et al.,* "First high-resolution tropospheric NO 2 observations from the ultraviolet visible hyperspectral imaging spectrometer," *Atmospheric Measurement Techniques,* vol. 14, no. 1, pp. 435-454, 2021.

[21] R. Gosselin, D. Rodrigue, and C. Duchesne, "A hyperspectral imaging sensor for on-line quality control of

extruded polymer composite products," *Computers & Chemical Engineering,* vol. 35, no. 2, pp. 296-306, 2011.

[22] R. F. Elhajjar, et al, "A hybrid numerical and imaging approach for characterizing defects in composite structures," *Composites Part A: Applied Science and Manufacturing,* vol. 81, pp. 98-104, 2016.

[23] B. Galdon-Navarro, et al, "Comparison of latent variable-based and artificial intelligence methods for impurity detection in PET recycling from NIR hyperspectral images," *J. of Chemometrics,* vol. 32, no. 1, e2980, 2018.

[24] S. Muroga, etc, "Near-infrared hyperspectral absorption/ scattering imaging method using multiple ground plates for evaluating polymer composites," *Analytical chemistry,* vol. 91, no. 3, pp. 1887-1893, 2018.

[25] A. Rinnan, F. Van Den Berg, and S. B. Engelsen, "Review of the most common pre-processing techniques for near-infrared spectra," *TrAC Trends in Analytical Chemistry,* vol. 28, no. 10, pp. 1201-1222, 2009.

[26] T. Qiao *et al.,* "Joint bilateral filtering and spectral similarity-based sparse representation," *Pattern Recog.,* vol. 77, pp. 316-328, 2018.

[27] C. Tomasi and R. Manduchi, "Bilateral filtering for gray and color images," in *6th Int. Conf. Computer Vision,* pp. 839-846, 1998.

[28] L. Van der Maaten etc, "Visualizing data using t-SNE," *J. of Machine Learning Research,* vol. 9, no. 11, 2008.

[29] M.-C. Tanzi, S. Fare, and G. Candiani, *Foundations of biomaterials engineering*. Academic Press, 2019.

[30] M. O. Seydibeyoglu, etc, *Fiber technology for fiber-reinforced composites.* Woodhead Publishing, 2017.

[31] Y. Yan *et al.,* "Unsupervised image saliency detection with Gestalt-laws guided optimization and visual attention based refinement," *Patt. Recog.,* vol. 79, pp. 65-78, 2018.

[32] E. Favarelli and A. Giorgetti, "Machine learning for automatic processing of modal analysis in damage detection of bridges," *IEEE Trans. Instrum. andMeasu.,* vol. 70, pp. 1-13, 2020.

[33] K. AGILUS. https://www.kuka.com/en-gb/products/robotics-systems/industrial-robots/kr-agilus. (accessed 11 Auguest 2021).

[34] P. Urhal, A. Weightman, C. Diver, and P. Bartolo, "Robot assisted additive manufacturing: A review," *Robotics and Computer-IntegratedManuf.,* vol. 59, pp. 335-345, 2019.

[35] S. Mousavi, V. Gagnol, B. C. Bouzgarrou, and P. Ray, "Dynamic modeling and stability prediction in robotic machining," *The Int. J. of Advanced Manufacturing Technology,* vol. 88, no. 9-12, pp. 3053-3065, 2017.

[36] B. Garcia-Garcia, etc, "Background subtraction in real applications: challenges, current models and future directions," *Comp. Sci. Review,* vol. 35, p. 100204, 2020.

[37] L. Deng, etc, "The effect of spatial resolution on radiometric and geometric performances of a UAV-mounted hyperspectral 2D imager," *ISPRS J. of Photog. and Remote Sens.,* vol. 144, pp. 298-314, 2018.

[38] J. Behmann *et al.,* "Specim IQ: evaluation of a new, miniaturized handheld hyperspectral camera and its application for plant phenotyping and disease detection," *Sensors,* vol. 18, no. 2, p. 441, 2018.

Yijun Yan (M'18) received the M.Sc. and Ph.D. degrees in electrical and electronic engineering from the University of Strathclyde, Glasgow, U.K. in 2013 and 2018, respectively. He is currently a Research Fellow with Robert Gordon University, Aberdeen, U.K. His research interests include HSI, pattern recognition, computer vision, and machine learning.

Jinchang Ren (M'07, SM'18) is a Professor of Computing Science with the National Subsea Centre, Robert Gordon University, Aberdeen, U.K. He received the B.E. degree in computer software, M.Eng. degree in image processing, and the D.Eng. degree in computer vision, all from Northwestern Polytechnical University, Xi'an, China, in 1992, 1997, and 2000, respectively, and also a Ph.D. degree in informatics from the University of Bradford, Bradford, U.K., in 2009. He His research interests cover hyperspectral imaging, image processing, computer vision, big data analytics, and machine learning.

Huan Zhao is a research associate in the University of Strathclyde. She received the B.Eng. degree from Hunan University of Science and Technology in 2009 and the M.Eng degree from Shenzhen University in 2012. She studied for her PhD in ultrasonics and signal processing, also at the University of Strathclyde.

James Windmill (M'99-SM'18) is a Professor, and Director of the Centre for Ultrasonic Engineering, in the Dept. of Electronic and Electrical Engineering, University of Strathclyde, Glasgow, U.K. He received a B.Eng. degree in electronic engineering in 1998 and a Ph.D. degree in magnetic microscopy in 2002, both from the University of Plymouth, UK. His research interests are in the field of biologically-inspired acoustic systems, from fundamental biology to various engineering application topics.

Winifred Ijomah is Professor in Sustainable Design and Manufacturing at the Dept. for Design, Manuf. and Engineering Management, University of Strathclyde. She is Director of the Scottish Institute for Remanufacturing, and Editor-in-Chief of Springer's Journal of Remanufacturing. Her work focuses on product end-of-life, particularly remanufacturing and spans both product and process design.

Jesper de Wit studied mechanical engineering with a focus on aircraft design and lightweight construction at the Technical University of Braunschweig, Germany (2004-2010). Employed as a test engineer at Volke GmbH, Wolfsburg, Germany, his career started in the automotive sector. Since 2022 he is employed as a project engineering manager services at Alstom Group.

Justus von Freeden joined the Fraunhofer Institute for Machine Tools and Forming Technology in 2016, after completing his master's degree at the Technical University of Braunschweig. His research interests include recycling, re-use and the concept of circular economy of composite material.